

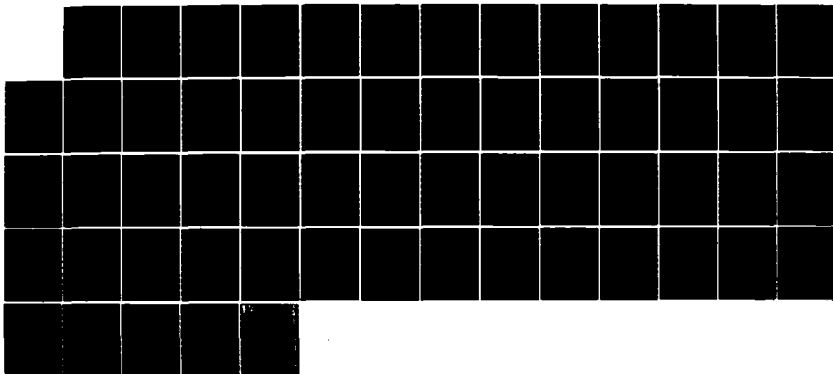
AD-A143 904

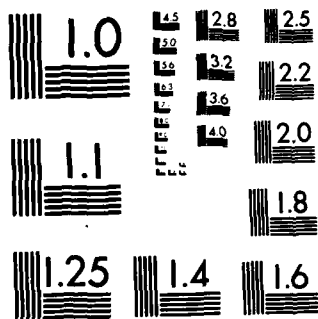
ACTA ARMAHENTARII (SELECTED ARTICLES)(U) FOREIGN
TECHNOLOGY DIV WRIGHT-PATTERSON AFB OH
W YUANYOU ET AL. 17 JUL 84 FTD-ID(RS)T-0611-84

1/1

UNCLASSIFIED

F/G 21/9.2 NL





MICROCOPY RESOLUTION TEST CHART
NATIONAL BUREAU OF STANDARDS-1963-A

AD-A143 904

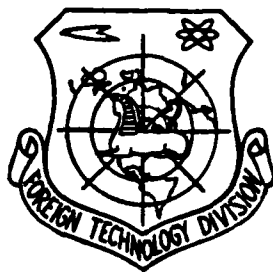
FTD-ID(RS)T-0611-84

2

FOREIGN TECHNOLOGY DIVISION



ACTA ARMAMENTARII
(Selected Articles)



DTIC
ELECTE
AUG 02 1984
S E D

DTIC FILE COPY

Approved for public release;
distribution unlimited.

84 7 31 170

EDITED TRANSLATION

FTD-ID(RS)T-0611-84

17 July 1984

MICROFICHE NR: FTD-84-C-000705

ACTA ARMAMENTARII (Selected Articles)

English pages: 54

Source: Binggong Xuebao, Nr. 3, August 1983,
pp. 20-33; 45-52; 53-59

Country of origin: China

Translated by: LEO KANNER ASSOCIATES
F33657-81-D-0264

Requester: FTD/TQTA

Approved for public release; distribution unlimited.

THIS TRANSLATION IS A RENDITION OF THE ORIGINAL FOREIGN TEXT WITHOUT ANY ANALYTICAL OR EDITORIAL COMMENT. STATEMENTS OR THEORIES ADVOCATED OR IMPLIED ARE THOSE OF THE SOURCE AND DO NOT NECESSARILY REFLECT THE POSITION OR OPINION OF THE FOREIGN TECHNOLOGY DIVISION.

PREPARED BY:

TRANSLATION DIVISION
FOREIGN TECHNOLOGY DIVISION
WP-AFB, OHIO.

Table of Contents

Graphics Disclaimer	ii
Viscoelastic Analysis of Stresses and Strains in Solid Propellant Grains Under Pressure Loadings, by W. Yuanyou	1
A Study of the Low Frequency Instability of the Solid Propellant Rocket Engine, by Z. Bohua	25
Ignition and Initial Pressure Peak of Small Solid Propellant Rocket Engines, by C. Hongzhang and J. Qingying	41

Accession For	
NTIS GRA&I	<input checked="" type="checkbox"/>
DTIC TAB	<input type="checkbox"/>
Unannounced	<input type="checkbox"/>
Justification	
By _____	
Distribution/	
Availability Codes	
Dist	Avail and/or Special
A1	



GRAPHICS DISCLAIMER

All figures, graphics, tables, equations, etc. merged into this translation were extracted from the best quality copy available.

VISCOELASTIC ANALYSIS OF STRESSES AND STRAINS IN SOLID PROPELLANT GRAINS UNDER PRESSURE LOADINGS

Wang Yuanyou

Abstract

This paper is a viscoelastic analysis of the stresses and strains caused by internal pressure loadings. Some engineering analysis methods already exist for solving this classical problem. For example, formulas were derived on the assumption that propellants are incompressible materials or overlooking the casing deformation. Although other calculation formulas do not make these assumptions yet Schapery's approximate inversions were used to obtain viscoelastic solutions. This paper proposes a new calculation method which does not use the above assumptions or the approximate inversions. Therefore, the solutions of the stresses and strains are more accurate than the above mentioned methods. This paper introduces two planar problems and their results under suddenly-applied pressure and gradually-applied pressure.

Symbols

a : inside radius of grain;
b : outside radius of grain;
c : outside radius of casing;
E : elastic constant;
k : stress concentration coefficient;
 k_i : stress concentration coefficient of inner hold ;
 P_i : internal pressure;
 E_g : propellant's glass modulus;
 E_c : propellant's rubber modulus;
 $E(t)$: propellant's relaxation modulus;
 $F(t)$: propellant's creep compliance;
 F_e : propellant's rubber compliance;
 F_g : propellant's glass compliance;
 $H(t) = \begin{cases} 1(t), & t \geq 0 \\ 0, & t < 0, \text{ unit step function;} \end{cases}$
h : thickness of casing wall;
 P' : contact pressure;

$$P = \sum_{i=0}^n a_i \frac{d^i}{dt^i},$$

$$Q = \sum_{i=0}^m b_i \frac{d^i}{dt^i},$$

r : radius of grain;
 u : radial displacement
 a : $f_a(\lambda, v)$ correlation parameter;
 β : $f_\beta(\lambda, v, v_c)$ correlation parameter;
 v : propellant's Poisson ratio;
 v_c : Poisson ratio of casing material.
 λ : b/a .

I. Introduction

During the ignition of a solid rocket engine, internal pressure can cause the inner surface of propellant grain to have cracks and thus possibly result in an engine ignition explosion accident. Therefore, it is necessary to carry out complete structural analysis of the grains. This necessitates precise calculations of the pressure and strain values caused by this type of load. At present, there already exist many engineering calculation methods: for example, the approximate solutions [1,2,6] obtained when the propellant is an incompressible material (Poisson ratio $v=0.5$); or the approximate solutions [3,5] obtained when the casing deformation is disregarded; in another method, although the above assumptions are not made yet Schapery's approximate inversions were used to obtain viscoelastic solutions. Although the first two methods can obtain simple calculation formulas, yet the calculation results tend to be low. Finally, because one type of method used Schapery's approximate inversions directly induced from the gradually varied process to handle this type of speed change of ignition, naturally, it was not accurate enough.

When deriving the viscoelastic solutions, this paper does not employ the above assumptions nor the approximate inversions

and thus the solutions obtained are more accurate. Moreover, if we assume that the propellant's Poisson ratio $\nu=0.5$, we can then derive the calculation formula of the first method from these results; if we disregard the casing deformation and take $E_a \rightarrow \infty$, we can then derive the calculation formula of the second method from these results. Therefore, the results of this paper are suitable for propellants with different Poisson ratios and also considers the deformation of the casing. This paper presents the final results of two loading situations, suddenly-applied pressure $P_i = P_i^0 H(t)$ and gradually-applied pressure $P_i = P_i^0 \cdot [1 - \exp(-nt)]$.

The following assumptions are made in this paper: (a) the propellant is an isotropic and homogeneous linear viscoelastic material; (b) the casing is a thin walled elastic small cylinder; (c) the Poisson ratio ν of the propellant is a constant; (d) the propellant grains and casings are relatively long and they are in a planar stress or planar strain state; (e) the influence of the shape of the inner hole is considered in terms of the stress concentration coefficient; (f) the inner hole boundary does not move, that is, we do not consider the ablation of the inner hole.

II. Elastic Solutions of Grain Stresses and Strains

The propellant is poured into a casing and therefore it involves the problem of analyzing the stresses and strains of two joined cylinders sustaining internal pressure. See Fig. 1.

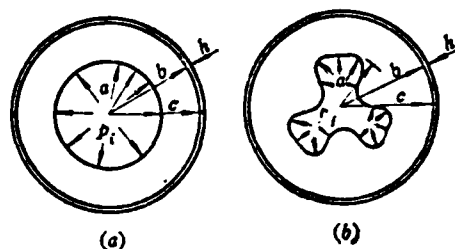


Fig. 1 Propellant grains.

Key: (a) Circular hole grain; (b) Star-shaped hole grain.

We will first study the circular hole grains. The engine is sufficiently long and thus the grain and casing are both in a planar stress or planar strain state. The specific structure of an engine possibly has the following conditions:

(1) The grain and casing are both in a planar strain state, that is, $\epsilon_z = \epsilon_{zc} = 0$;

(2) The grain is in a common planar stress state and the casing is in a planar strain state, that is $\sigma_z = -P_i, \epsilon_{zc} = 0$.

It is generally considered that an engine with cohesion of the two ends of the grain and the casing is close to the first type of condition; an engine with non-cohesion (free) of the two ends of the grain is close to the second condition. We separately study the solutions under both conditions.

The boundary conditions of the two conditions are shown in Table 1.

	情况 ①	情况 ②
$r = a$	$\sigma_r(a) = -P_i$	$\sigma_r(a) = -P_i$
$r = b$	$u(b) = u_c(b)$	$u(b) = u_c(b)$
$r = c$	$\sigma_{re}(c) = 0$	$\sigma_{re}(c) = 0$
$z = 0, l$	$\epsilon_z = \epsilon_{zc} = 0$	$\sigma_z = -P_i, \epsilon_{zc} = 0$

Table 1

Key: (1)-(2) Condition.

Because the deformation of the grain (inner cylinder) is constrained by the casing (outer cylinder), contact pressure P' will be produced on their connecting surfaces. The contact pressure can be determined based on boundary condition $u(b) = u_c(b)$ listed in the table.

Under the first type of condition, we obtain

$$P' = \frac{2(1-\nu)a^2P_i}{[a^2 + (1-2\nu)b^2] + \frac{b^2-a^2}{c^2-b^2} \frac{1+\nu_c}{1+\nu} \frac{E}{E_c} [c^2 + (1-2\nu_c)b^2]} \quad (1)$$

As regards the thin walled casing, $h/b \ll 1$, and the above formula can be simplified to

$$P' = \frac{2(1-\nu)P_i}{(1+(1-2\nu)\lambda^2) + (\lambda^2-1) \frac{1-\nu^2}{1+\nu} \frac{b}{h} \frac{E}{E_s}} \quad (2)$$

Under the second type of condition, we obtain

$$P' = \frac{(2a^2 + (b^2 - a^2)\nu)P_i}{((1+\nu)a^2 + (1-\nu)b^2) + \frac{b^2 - a^2}{c^2 - b^2}(1+\nu_s) \frac{E}{E_s} ((1-2\nu_s)b^2 + c^2)} \quad (3)$$

As regards the thin walled casing, the above formula can be simplified to

$$P' = \frac{(2 + (\lambda^2 - 1)\nu)P_i}{((1+\nu) + (1-\nu)\lambda^2) + (\lambda^2 - 1)(1-\nu^2) \frac{b}{h} \frac{E}{E_s}} \quad (4)$$

The last term of the denominators of formulas (1)-(4) show the influence of the casing's rigidity. Often $E/E_c \ll 1$ and this term is a minute quantity. Therefore, we can use the Taylor series to expand the contact pressure formula into a polynomial expression and disregard the minute quantities of high order. For example, after expansion of formula (2), we can obtain

$$\begin{aligned} P' &\approx \frac{2(1-\nu)}{1+(1-2\nu)\lambda^2} P_i - \frac{2(\lambda^2-1)}{[1+(1-2\nu)\lambda^2]^2} \frac{1-\nu}{1+\nu} (1-\nu^2) \frac{b}{h} \frac{E}{E_s} P_i \\ &= \alpha_1 P_i - \beta_1 \frac{b}{h} \frac{E}{E_s} P_i = \alpha_1 P_i - P'' \end{aligned} \quad (5)$$

In the formula

$$P'' = \beta_1 \frac{b}{h} \frac{E}{E_s} P_i \quad (6)$$

$$\left. \begin{aligned} \alpha_1 &= \frac{2(1-\nu)}{1+(1-2\nu)\lambda^2} \\ \beta_1 &= \frac{2(\lambda^2-1)}{[1+(1-2\nu)\lambda^2]^2} \frac{1-\nu}{1+\nu} (1-\nu^2) \end{aligned} \right\} \quad (7)$$

In the same way, after expanding formula (4) under the second type of condition, we can obtain

$$P' \approx \frac{2 + (\lambda^2 - 1)v}{1 + v + (1 - v)\lambda^2} P_i - \frac{[2 + (\lambda^2 - 1)v](\lambda^2 - 1)}{[1 + v + (1 - v)\lambda^2]^2} (1 - v^2) \frac{b}{h} \frac{E}{E_s} P_i$$

$$= \alpha_1 P_i - \beta_1 \frac{b}{h} \frac{E}{E_s} P_i = \alpha_1 P_i - P'' \quad (8)$$

In the formula

$$P'' = \beta_2 \frac{b}{h} \frac{E}{E_s} P_i \quad (9)$$

$$\left. \begin{aligned} \alpha_1 &= \frac{2 + (\lambda^2 - 1)v}{1 + v + (1 - v)\lambda^2} \\ \beta_1 &= \frac{[2 + (\lambda^2 - 1)v](\lambda^2 - 1)}{[1 + v + (1 - v)\lambda^2]^2} (1 - v^2) \end{aligned} \right\} \quad (10)$$

It can be seen that under the two conditions, the relationship between contact pressure P' and internal pressure P_i can be expressed as

$$P' = \alpha P_i - P'' \quad (11)$$

$$P'' = \beta \frac{b}{h} \frac{E}{E_s} P_i \quad (11)'$$

We can see from formulas (7) and (10) that aside from being related to the stress-strain condition, the values of α and β are mainly determined by Poisson ratios v, v_c and λ . Based on the assumptions discussed in the introduction, α and β are constants and when $v=0.5$, $\alpha=1$.

After contact pressure P' is known, by substituting P' into the Lamé formula, we can obtain the stress value:

$$\sigma_r = -\frac{\lambda^2}{\lambda^2 - 1} \left[\left(1 - \frac{a^2}{r^2} \right) \alpha + \frac{1}{\lambda^2} \left(\frac{b^2}{r^2} - 1 \right) \right] P_i + \frac{\lambda^2}{\lambda^2 - 1} \left(1 - \frac{a^2}{r^2} \right) P'' \quad (12)$$

$$\sigma_t = -\frac{\lambda^2}{\lambda^2 - 1} \left[\left(1 + \frac{a^2}{r^2} \right) \alpha - \frac{1}{\lambda^2} \left(\frac{b^2}{r^2} + 1 \right) \right] P_i + \frac{\lambda^2}{\lambda^2 - 1} \left(1 + \frac{a^2}{r^2} \right) P'' \quad (13)$$

As regards incompressible material ($v=0.5$), because $\alpha=1$, the coefficients of the first terms in formulas (12) and (13) are equal to -1 and can thus be simplified to

$$\sigma_r = -P_i + \frac{\lambda^2}{\lambda^2 - 1} \left(1 - \frac{a^2}{r^2} \right) P'' \quad (12)'$$

$$\sigma_\theta = -P_i + \frac{\lambda^2}{\lambda^2 - 1} \left(1 + \frac{a^2}{r^2} \right) P'' \quad (13)'$$

By substituting the known stress into the strain formula, we can then separately obtain the strain values and the two types of conditions.

Under the first type of condition

$$\begin{aligned} \epsilon_r &= \frac{1-\nu^2}{E} \left(\sigma_r - \frac{\nu}{1-\nu} \sigma_\theta \right) \\ &= \frac{-(1-2\nu)(1+\nu)}{1+(1-2\nu)\lambda^2} \left(\frac{b^2}{r^2} + 1 \right) \frac{P_i}{E} + \frac{\lambda^2(1+\nu)}{\lambda^2-1} \left[(1-2\nu) - \frac{a^2}{r^2} \right] \frac{P''}{E} \end{aligned} \quad (14)$$

$$\begin{aligned} \epsilon_\theta &= \frac{1-\nu^2}{E} \left(\sigma_\theta - \frac{\nu}{1-\nu} \sigma_r \right) \\ &= \frac{(1-2\nu)(1+\nu)}{1+(1-2\nu)\lambda^2} \left(\frac{b^2}{r^2} - 1 \right) \frac{P_i}{E} + \frac{\lambda^2(1+\nu)}{\lambda^2-1} \left[(1-2\nu) + \frac{a^2}{r^2} \right] \frac{P''}{E} \end{aligned} \quad (15)$$

Under the second type of condition

$$\begin{aligned} \epsilon_r &= \frac{1}{E} (\sigma_r - \nu \sigma_\theta + \nu P_i) \\ &= \left\{ \frac{1}{\lambda^2-1} \left[(1-\nu)(1-\alpha\lambda^2) - (1+\nu)(1-\alpha) \frac{b^2}{r^2} \right] + \nu \right\} \frac{P_i}{E} \\ &\quad + \frac{\lambda^2}{\lambda^2-1} \left[(1-\nu) - (1+\nu) \frac{a^2}{r^2} \right] \frac{P''}{E} \end{aligned} \quad (16)$$

$$\begin{aligned} \epsilon_\theta &= \frac{1}{E} (\sigma_\theta - \nu \sigma_r + \nu P_i) \\ &= \left\{ \frac{1}{\lambda^2-1} \left[(1-\nu)(1-\alpha\lambda^2) + (1+\nu)(1-\alpha) \frac{b^2}{r^2} \right] + \nu \right\} \frac{P_i}{E} \\ &\quad + \frac{\lambda^2}{\lambda^2-1} \left[(1-\nu) + (1+\nu) \frac{a^2}{r^2} \right] \frac{P''}{E} \end{aligned} \quad (17)$$

We can see from stress formulas (12) and (13) and strain formulas (14)-(17) that: under the two above mentioned types of conditions, $\sigma_\theta > \sigma_r$ and $\varepsilon_\theta > \varepsilon_r$. Moreover, their maximum values occur on the inner surface ($r=a$), that is, $\sigma_{\max} = \sigma_\theta(a)$ and $\varepsilon_{\max} = \varepsilon_\theta(a)$.

Below, we will study the elastic solutions of the stresses and strains of grains with star-shaped holes.

When we carry out a complete analysis of the grain structures, we pay close attention to the maximum values of the stresses and strains. We already pointed out above that the maximum stresses and strains of grains with circular holes occur on the inner surface while in star-shaped grains the inner hole star-shaped angles have the most serious stress concentration. Therefore, the stresses and strains of grains with star-shaped holes are maximum in the inner hole star-shaped angle areas. We record the stress's maximum value as $\sigma_\theta^*(a, t)$ and the strain's maximum value as $\varepsilon_\theta^*(a, t)$. The upper symbol * represents the value of the grains with star-shaped holes and no upper symbol represents the value of equivalent grains with circular holes. The stress concentration coefficient is defined as

$$k = \frac{\sigma_r^* - \sigma_\theta^*}{\sigma_r - \sigma_\theta}$$

As regards the inner hole

$$\sigma_r^*(a) - \sigma_\theta^*(a) = k[\sigma_r(a) - \sigma_\theta(a)] \quad (18)$$

In the formula, $\sigma_r^*(a) = -P_i$ and the stress difference of equivalent grains with circular holes is

$$\sigma_r(a) - \sigma_\theta(a) = \frac{-2\lambda^2}{\lambda^2 - 1}(P_i - P') = \frac{-2\lambda^2}{\lambda^2 - 1}[(1 - \alpha)P_i + P''] \quad (19)$$

By substituting in formula (18), we obtain

$$\sigma_\theta^*(a) = \frac{2\lambda^2}{\lambda^2 - 1} k[(1 - \alpha)P_i + P''] - P_i \quad (20)$$

Below, we will present maximum strain $\varepsilon_\theta^*(a)$:

Under the first type of condition

$$\begin{aligned}\epsilon_0^*(a) &= \frac{1-v^2}{E} \left[\sigma_0^*(a) - \frac{v}{1-v} \sigma_r^*(a) \right] \\ &= \frac{1-v^2}{E} \left[\frac{2\lambda^2}{\lambda^2-1} k_i(1-a) - \frac{1-2v}{1-v} \right] P_i + \frac{1-v^2}{E} \frac{2\lambda^2}{\lambda^2-1} k_i P''\end{aligned}\quad (21)$$

Under the second type of condition

$$\begin{aligned}\epsilon_0^*(a) &= \frac{1}{E} [\sigma_0^*(a) - v\sigma_r^*(a) + vP_i] \\ &= \frac{1}{E} \left[\frac{2\lambda^2}{\lambda^2-1} k_i(1-a) - (1-2v) \right] P_i + \frac{1}{E} \frac{2\lambda^2}{\lambda^2-1} k_i P''\end{aligned}\quad (22)$$

III. Viscoelastic Solutions For the Stresses and Strains of Grains

After attaining the elastic solution, by employing the correspondence principle in viscoelastic mechanics, we can obtain the Laplace transform of the viscoelastic solutions and then obtain the viscoelastic solutions by inverse Laplace transformation.

WE used the finite element generalized Maxwell model to represent the mechanical properties of the propellant [8] as shown in Fig. 2.

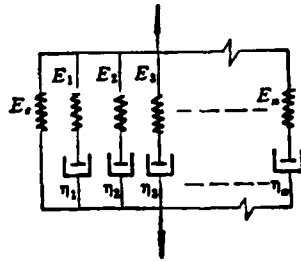


Fig. 2 Generalized Maxwell model.

The Laplace transformation of the operator modulus is

$$\frac{\bar{Q}(s)}{\bar{P}(s)} = E_0 + \sum_{i=1}^N \frac{E_i s}{s + \frac{1}{\tau_i}} \quad (23)$$

The relaxation modulus is expressed by the Prony series

$$\left. \begin{aligned} E(t) &= E_* + \sum_{i=1}^N E_i \exp\left(-\frac{t}{\tau_i}\right) \\ E_* &= E(0) = E_* + \sum_{i=1}^N E_i \end{aligned} \right\} \quad (24)$$

In the formula, N is the Maxwell element number; τ_i is the relaxation time $\left(= \frac{\eta_i}{E_i}\right)$.

We first find the viscoelastic solution $P'(t)$ of contact pressure P' . The Laplace transform of formula (11) is

$$\bar{P}'(s) = \alpha \bar{P}_i(s) - \bar{P}''(s) \quad (25)$$

If we use the differential operator to express the constitutive equations, based on the correspondence principle, from formula (11) we obtain

$$\bar{P}''(s) = \beta \frac{b}{h} \frac{1}{E_*} \frac{\bar{Q}(s)}{\bar{P}(s)} \bar{P}_i(s) \quad (26)$$

When using the integral operator to express the constitutive equations, then

$$\bar{P}''(s) = \beta \frac{b}{h} \frac{1}{E_*} s \bar{E}(s) \bar{P}_i(s) \quad (27)$$

Below, we will discuss the solutions of classical pressurization equations:

As regards suddenly-applied pressure wherein the internal pressure is a step function $P_i = P_i^0 H(t)$, at this time $\bar{P}_i(s) = P_i^0/s$. By substituting in formula (27), we obtain

$\bar{P}''(s) = \beta \frac{b}{h} \frac{1}{E_*} \bar{E}(s) P_i^0$, and then seek the inverse and obtain

$$P''(t) = \beta \frac{b}{h} \frac{E(t)}{E_*} P_i^0 \quad (28)$$

Therefore

$$P'(t) = \alpha P_i^0 H(t) - \beta \frac{b}{h} \frac{E(t)}{E_*} P_i^0 \quad (29)$$

In the formula, $E(t)$ can directly use the measured value.

As regards the gradually-applied pressure, $P_i = P_i^0 [1 - \exp(-nt)]$, and at this time

$$\bar{P}_i(s) = P_i^0 \cdot \frac{n}{s(s+n)} \quad (30)$$

We substitute formulas (30) and (23) into formula (26) and obtain

$$\bar{P}''(s) = \beta \frac{b}{h} \frac{P_i^0}{E_*} \left[E_* \frac{n}{s(s+n)} + \sum_{i=1}^N \frac{nE_i}{(s+n) \left(s + \frac{1}{\tau_i} \right)} \right]$$

Seeking the inverse, we obtain

$$P''(t) = \beta \frac{b}{h} \frac{E_*}{E_*} P_i^0 f_s(t) \quad (31)$$

In the formula

$$f_s(t) = 1 - e^{-nt} + \sum_{i=1}^N \frac{n\tau_i}{n\tau_i - 1} \frac{E_i}{E_*} \left(e^{-\frac{t}{\tau_i}} - e^{-nt} \right) \quad (32)$$

Therefore

$$P'(t) = \alpha P_i^0 (1 - e^{-nt}) - \beta \frac{b}{h} \frac{E_*}{E_*} P_i^0 f_s(t) \quad (33)$$

If we substitute formula (30) into formula (27) in the same way we can obtain formulas (31) and (33). At this time, auxiliary function $f_E(t)$ is expressed as an integral form and we can calculate using the measured $E(t)$ value:

$$f_s(t) = \frac{n}{E_*} e^{-nt} \int_0^t E(\tau) e^{n\tau} d\tau \quad (32)'$$

By substituting derived pressure $P''(t)$ into stress formulas (12) and (13) we can find the viscoelastic solution of the stress:

As regards the suddenly-applied pressure

$$\frac{\sigma_r(r, t)}{P_i^0} = \frac{-\lambda^2}{\lambda^2 - 1} \left[\left(1 - \frac{a^2}{r^2} \right) \alpha + \frac{1}{\lambda^2} \left(\frac{b^2}{r^2} - 1 \right) \right] + \frac{\lambda^2}{\lambda^2 - 1} \left(1 - \frac{a^2}{r^2} \right) \cdot \beta \frac{b}{h} \frac{E(t)}{E_s} \quad (34)$$

$$\frac{\sigma_\theta(r, t)}{P_i^0} = \frac{-\lambda^2}{\lambda^2 - 1} \left[\left(1 + \frac{a^2}{r^2} \right) \alpha - \frac{1}{\lambda^2} \left(\frac{b^2}{r^2} + 1 \right) \right] + \frac{\lambda^2}{\lambda^2 - 1} \left(1 + \frac{a^2}{r^2} \right) \cdot \beta \frac{b}{h} \frac{E(t)}{E_s} \quad (35)$$

Therefore

$$\frac{\sigma_{\max}}{P_i^0} = \frac{\sigma_\theta(a, t)}{P_i^0} = \frac{-1}{\lambda^2 - 1} (\lambda^2(2\alpha - 1) - 1) + \frac{2\lambda^2}{\lambda^2 - 1} \beta \frac{b}{h} \frac{E(t)}{E_s} \quad (36)$$

As regards the gradually-applied pressure

$$\frac{\sigma_r(r, t)}{P_i^0} = \frac{-\lambda^2}{\lambda^2 - 1} \left[\left(1 - \frac{a^2}{r^2} \right) \alpha + \frac{1}{\lambda^2} \left(\frac{b^2}{r^2} - 1 \right) \right] (1 - e^{-\alpha t}) + \frac{\lambda^2}{\lambda^2 - 1} \left(1 - \frac{a^2}{r^2} \right) \beta \frac{b}{h} \frac{E_s}{E_s} f_\varepsilon(t) \quad (37)$$

$$\frac{\sigma_\theta(r, t)}{P_i^0} = \frac{-\lambda^2}{\lambda^2 - 1} \left[\left(1 + \frac{a^2}{r^2} \right) \alpha - \frac{1}{\lambda^2} \left(\frac{b^2}{r^2} + 1 \right) \right] (1 - e^{-\alpha t}) + \frac{\lambda^2}{\lambda^2 - 1} \left(1 + \frac{a^2}{r^2} \right) \beta \frac{b}{h} \frac{E_s}{E_s} f_\varepsilon(t) \quad (38)$$

Therefore

$$\frac{\sigma_{\max}}{P_i^0} = \frac{\sigma_\theta(a, t)}{P_i^0} = \frac{-1}{\lambda^2 - 1} (\lambda^2(2\alpha - 1) - 1) (1 - e^{-\alpha t}) + \frac{2\lambda^2}{\lambda^2 - 1} \beta \frac{b}{h} \frac{E_s}{E_s} f_\varepsilon(t) \quad (39)$$

Below, we will study the viscoelastic solutions of the strains. For convenience of calculation, we used the finite element generalized Voigt model to represent the mechanical properties of the propellant [8] as shown in Fig. 3.

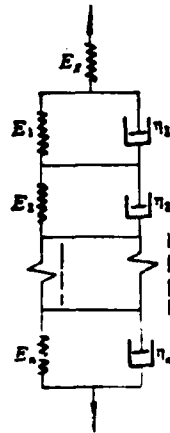


Fig. 3 Generalized Voigt model.

The Laplace transform of the operator compliance is

$$\frac{\bar{P}(s)}{\bar{Q}(s)} = F_s + \sum_{i=1}^N F_i \frac{1}{\tau_i \left(s + \frac{1}{\tau_i} \right)} \quad (40)$$

The creep compliance is expressed as the Prony series

$$\left. \begin{aligned} F(t) &= F_s + \sum_{i=1}^N F_i \left[1 - \exp \left(- \frac{t}{\tau_i} \right) \right] \\ F_s &= F_s + \sum_{i=1}^N F_i \end{aligned} \right\} \quad (41)$$

In the formula, N is the Voigt element number; τ_i is the delay time ($= \frac{\eta_i}{E_i}$).

Under the first type of condition, we substituted formula (11)' into formulas (14) and (15) and used the corresponding principle to obtain

$$\bar{\varepsilon}_r(s) = -\frac{(1-2\nu)(1+\nu)}{1+(1-2\nu)\lambda^2} \left(\frac{b^2}{r^2} + 1 \right) \frac{\bar{P}(s)}{Q(s)} \bar{P}_i(s) + \frac{\lambda^2(1+\nu)}{\lambda^2-1} \left[(1-2\nu) - \frac{a^2}{r^2} \right] \beta \frac{b}{h} \frac{1}{E_*} \bar{P}_i(s) \quad (42)$$

$$\bar{\varepsilon}_\theta(s) = \frac{(1-2\nu)(1+\nu)}{1+(1-2\nu)\lambda^2} \left(\frac{b^2}{r^2} - 1 \right) \frac{\bar{P}(s)}{Q(s)} \bar{P}_i(s) + \frac{\lambda^2(1+\nu)}{\lambda^2-1} \left[(1-2\nu) + \frac{a^2}{r^2} \right] \beta \frac{b}{h} \frac{1}{E_*} \bar{P}_i(s) \quad (43)$$

If we use the integral operator to express the constitutive equations, then

$$\bar{\varepsilon}_r(s) = -\frac{(1-2\nu)(1+\nu)}{1+(1-2\nu)\lambda^2} \left(\frac{b^2}{r^2} + 1 \right) s\bar{F}(s) \bar{P}_i(s) + \frac{\lambda^2(1+\nu)}{\lambda^2-1} \left[(1-2\nu) - \frac{a^2}{r^2} \right] \beta \frac{b}{h} \frac{1}{E_*} \bar{P}_i(s) \quad (42)'$$

$$\bar{\varepsilon}_\theta(s) = \frac{(1-2\nu)(1+\nu)}{1+(1-2\nu)\lambda^2} \left(\frac{b^2}{r^2} - 1 \right) s\bar{F}(s) \bar{P}_i(s) + \frac{\lambda^2(1+\nu)}{\lambda^2-1} \left[(1-2\nu) + \frac{a^2}{r^2} \right] \beta \frac{b}{h} \frac{1}{E_*} \bar{P}_i(s) \quad (43)'$$

$$P_i = P_i^0 H(t),$$

As regards the suddenly-applied pressure, we substitute $\Lambda \bar{P}_i(s) = P_i^0/s$ into formulas (42)' and (43)', seek the inverse and obtain

$$\frac{\varepsilon_r(r, t)}{P_i^0} = -\frac{(1-2\nu)(1+\nu)}{1+(1-2\nu)\lambda^2} \left(\frac{b^2}{r^2} + 1 \right) F(t) + \frac{\lambda^2(1+\nu)}{\lambda^2-1} \left[(1-2\nu) - \frac{a^2}{r^2} \right] \beta \frac{b}{h} \frac{1}{E_*} \quad (44)$$

$$\frac{\varepsilon_\theta(r, t)}{P_i^0} = \frac{(1-2\nu)(1+\nu)}{1+(1-2\nu)\lambda^2} \left(\frac{b^2}{r^2} - 1 \right) F(t) + \frac{\lambda^2(1+\nu)}{\lambda^2-1} \left[(1-2\nu) + \frac{a^2}{r^2} \right] \beta \frac{b}{h} \frac{1}{E_*} \quad (45)$$

$$\frac{\varepsilon_{\max}}{P_i^0} = \frac{\varepsilon_\theta(a, t)}{P_i^0} = \frac{(1-2\nu)(1+\nu)(\lambda^2-1)}{1+(1-2\nu)\lambda^2} F(t) + \frac{2\lambda^2}{\lambda^2-1} (1-\nu^2) \beta \frac{b}{h} \frac{1}{E_*} \quad (46)$$

As regards the gradually-applied pressure, we substitute $P_i = P_i^0 [1 - \exp(-nt)]$ and $\bar{P}_i(s) = P_i^0 \frac{n}{s(s+n)}$ into formulas (42) and (43), consider formula (40), then seek the inverse and obtain

$$\begin{aligned} \frac{\varepsilon_r(r, t)}{P_i^0} = & -\frac{(1-2\nu)(1+\nu)}{1+(1-2\nu)\lambda^2} \left(\frac{b^2}{r^2} + 1 \right) \frac{1}{E_s} f_r(t) \\ & + \frac{\lambda^2(1+\nu)}{\lambda^2-1} \left[(1-2\nu) - \frac{a^2}{r^2} \right] \beta \frac{b}{h} \frac{1}{E_s} (1 - e^{-nt}) \end{aligned} \quad (47)$$

$$\begin{aligned} \frac{\varepsilon_\theta(r, t)}{P_i^0} = & -\frac{(1-2\nu)(1+\nu)}{1+(1-2\nu)\lambda^2} \left(\frac{b^2}{r^2} - 1 \right) \frac{1}{E_s} f_r(t) + \frac{\lambda^2(1+\nu)}{\lambda^2-1} \left[(1-2\nu) \right. \\ & \left. + \frac{a^2}{r^2} \right] \beta \frac{b}{h} \frac{1}{E_s} (1 - e^{-nt}) \end{aligned} \quad (48)$$

$$\begin{aligned} \frac{\varepsilon_{max}}{P_i^0} = \frac{\varepsilon_\theta(a, t)}{P_i^0} = & \frac{(1-2\nu)(1+\nu)}{1+(1-2\nu)\lambda^2} (\lambda^2 - 1) \frac{1}{E_s} f_r(t) \\ & + \frac{2\lambda^2(1-\nu^2)}{\lambda^2-1} \beta \frac{b}{h} \frac{1}{E_s} (1 - e^{-nt}) \end{aligned} \quad (49)$$

In the formula, auxiliary function

$$f_r(t) = 1 - e^{-nt} + \sum_{i=1}^N \frac{F_i}{F_s} \left(1 + \frac{e^{-nt}}{n\tau_i - 1} - \frac{n\tau_i e^{-\frac{t}{\tau_i}}}{n\tau_i - 1} \right) \quad (50)$$

If we substitute the Laplace transform of the internal pressure into formulas (42)' and (43)', in the same way we can obtain formulas (47), (48) and (49), only the auxiliary function is

$$f_r(t) = nE_s e^{-nt} \int_0^t F(\tau) e^{n\tau} d\tau \quad (50)'$$

At this time, we can directly use the measured value of creep compliance $F(t)$ for calculations.

In the same way, we can find viscoelastic solutions of the strains under the second type of condition. As regards suddenly-applied pressure $P_i = P_i^0 H(t)$

$$\frac{\varepsilon_r(r, t)}{P_i^0} = \left\{ \frac{1}{\lambda^2 - 1} \left[(1 - \nu)(1 - \alpha\lambda^2) - (1 + \nu)(1 - \alpha) \frac{b^2}{r^2} \right] + \nu \right\} F(t) + \frac{\lambda^2}{\lambda^2 - 1} \left[(1 - \nu) - (1 + \nu) \frac{a^2}{r^2} \right] \beta \frac{b}{h} \frac{1}{E_s} \quad (51)$$

$$\frac{\varepsilon_\theta(r, t)}{P_i^0} = \left\{ \frac{1}{\lambda^2 - 1} \left[(1 - \nu)(1 - \alpha\lambda^2) + (1 + \nu)(1 - \alpha) \frac{b^2}{r^2} \right] + \nu \right\} F(t) + \frac{\lambda^2}{\lambda^2 - 1} \left[(1 - \nu) + (1 + \nu) \frac{a^2}{r^2} \right] \beta \frac{b}{h} \frac{1}{E_s} \quad (52)$$

$$\frac{\varepsilon_{\max}}{P_i^0} = \frac{\varepsilon_\theta(a, t)}{P_i^0} = \left\{ \frac{1}{\lambda^2 - 1} \left[(1 - \nu)(1 - \alpha\lambda^2) + (1 + \nu)(1 - \alpha)\lambda^2 \right] + \nu \right\} F(t) + \frac{2\lambda^2}{\lambda^2 - 1} \beta \frac{b}{h} \frac{1}{E_s} \quad (53)$$

As regards gradually-applied pressure $P_i = P_i^0 [1 - \exp(-nt)]$:

$$\frac{\varepsilon_r(r, t)}{P_i^0} = \left\{ \frac{1}{\lambda^2 - 1} \left[(1 - \nu)(1 - \alpha\lambda^2) - (1 + \nu)(1 - \alpha) \frac{b^2}{r^2} \right] + \nu \right\} \frac{1}{E_s} f_r(t) + \frac{\lambda^2}{\lambda^2 - 1} \left[(1 - \nu) - (1 + \nu) \frac{a^2}{r^2} \right] \beta \frac{b}{h} \frac{1}{E_s} (1 - e^{-nt}) \quad (54)$$

$$\frac{\varepsilon_\theta(r, t)}{P_i^0} = \left\{ \frac{1}{\lambda^2 - 1} \left[(1 - \nu)(1 - \alpha\lambda^2) + (1 + \nu)(1 - \alpha) \frac{b^2}{r^2} \right] + \nu \right\} \frac{1}{E_s} f_r(t) + \frac{\lambda^2}{\lambda^2 - 1} \left[(1 - \nu) + (1 + \nu) \frac{a^2}{r^2} \right] \beta \frac{b}{h} \frac{1}{E_s} (1 - e^{-nt}) \quad (55)$$

$$\frac{\varepsilon_{\max}}{P_i^0} = \frac{\varepsilon_\theta(a, t)}{P_i^0} = \left\{ \frac{1}{\lambda^2 - 1} \left[(1 - \nu)(1 - \alpha\lambda^2) + (1 + \nu)(1 - \alpha)\lambda^2 \right] + \nu \right\} \frac{1}{E_s} f_r(t) + \frac{2\lambda^2}{\lambda^2 - 1} \beta \frac{b}{h} \frac{1}{E_s} (1 - e^{-nt}) \quad (56)$$

In the above formulas, the definition of auxiliary function $f_F(t)$ is the same as in formulas (50) and (50)'. The above are viscoelastic solutions of the stresses and strains of grains with circular holes.

Below, we will study the viscoelastic solutions of the stresses and strains of grains with star-shaped holes. For these types of grains, it is only necessary to derive maximum stress $\sigma_\theta^*(a, t)$ and maximum strain $\varepsilon_\theta^*(a, t)$.

By substituting formula (28) into formula (20), we can

obtain stress $\sigma_{\theta}^*(a, t)$ under suddenly-applied pressure

$$\frac{\sigma_{\theta}^*(a, t)}{P_i^0} = \frac{2\lambda^2}{\lambda^2 - 1} k_i \left[(1 - \alpha) + \beta \frac{b}{h} \frac{E(t)}{E_s} \right] - 1 \quad (57)$$

By substituting formula (31) into formula (20), we can obtain stress $\sigma_{\theta}^*(a, t)$ under gradually-applied pressure

$$\frac{\sigma_{\theta}^*(a, t)}{P_i^0} = \frac{2\lambda^2}{\lambda^2 - 1} k_i \left[(1 - \alpha)(1 - e^{-nt}) + \beta \frac{b}{h} \frac{E_s}{E_s} f_s(t) \right] - (1 - e^{-nt}) \quad (58)$$

Based on elastic solution formulas (21) and (22) for the stress and using the correspondence principle, we can find maximum strain $\varepsilon_{\theta}^*(a, t)$ under the two types of conditions:

Under the first type of condition, as regards suddenly-applied pressure $P_i = P_i^0 H(t)$

$$\begin{aligned} \frac{\varepsilon_{\theta}^*(a, t)}{P_i^0} &= (1 - \nu^2) \left[\frac{2\lambda^2}{\lambda^2 - 1} k_i (1 - \alpha) - \frac{1 - 2\nu}{1 - \nu} \right] F(t) \\ &+ (1 - \nu^2) \frac{2\lambda^2}{\lambda^2 - 1} k_i \beta \frac{b}{h} \frac{1}{E_s} \end{aligned} \quad (59)$$

As regards gradually-applied pressure $P_i = P_i^0 [1 - \exp(-nt)]$

$$\begin{aligned} \frac{\varepsilon_{\theta}^*(a, t)}{P_i^0} &= (1 - \nu^2) \left[\frac{2\lambda^2}{\lambda^2 - 1} k_i (1 - \alpha) - \frac{1 - 2\nu}{1 - \nu} \right] \frac{1}{E_s} f_r(t) \\ &+ (1 - \nu^2) \frac{2\lambda^2}{\lambda^2 - 1} k_i \beta \frac{b}{h} \frac{1}{E_s} (1 - e^{-nt}) \end{aligned} \quad (60)$$

Under the second type of condition, as regards the suddenly-applied pressure

$$\frac{\varepsilon_{\theta}^*(a, t)}{P_i^0} = \left[\frac{2\lambda^2}{\lambda^2 - 1} k_i (1 - \alpha) - (1 - 2\nu) \right] F(t) + \frac{2\lambda^2}{\lambda^2 - 1} k_i \beta \frac{b}{h} \frac{1}{E_s} \quad (61)$$

As regards the gradually-applied pressure

$$\frac{\sigma_{\theta}^*(a, t)}{P_i^0} = \left[\frac{2\lambda^2}{\lambda^2 - 1} k_i(1 - \alpha) - (1 - 2\nu) \right] \frac{1}{E_s} f_r(t) + \frac{2\lambda^2}{\lambda^2 - 1} k_i \beta \frac{b}{h} \cdot \frac{1}{E_s} (1 - e^{-\alpha t}) \quad (62)$$

Naturally, if the propellant is an incompressible material ($\nu=0.5$) and $\alpha=1$, then formulas (57)-(62) above are simplified into simple calculation formulas [2].

Below, we will use the above mentioned calculation formulas to carry out calculation and analysis of specific propellant grains.

Grain dimensions: outer radius $b=30\text{cm}$, inner radius $a=15.8\text{cm}$, the star-shaped angle number is 5, the star-shaped angle coefficient is 0.8 and transition circular arc radius $\rho=1.5\text{cm}$, the thin walled steel casing: $E_c=2 \times 10^6 \text{kg/cm}^2$, Poisson ratio $\nu_c=1/3$, wall thickness $h=0.3\text{cm}$; the propellant's relaxation modulus $E(t)=14.0+7.25\exp(-t/0.002)+404.70\exp(-t/0.02)+109.91\exp(-t/0.2)+500.82\exp(-t/2)$, $E_g=1037\text{kg/cm}^2$, $E_e=14\text{kg/cm}^2$, Poisson ratio $\nu=0.48$; the combustion chamber's equilibrium pressure $P_i^0=70\text{kg/cm}^2$ and transition pressure $P_i=70[1-\exp(-60t)]$.

1. Calculation results of suddenly-applied pressure $P_i=P_i^0 H(t)=70\text{kg/cm}^2$:

We used formula (57) to calculate maximum stress $\sigma_{\theta}^*(a, t)$ under two types of conditions as shown in Table 2:

$t(s)$		0	0.01	0.03	0.05	0.07	0.09	0.10	1
$\sigma_{\theta}^*(a, t)$	情况①	0.168	0.088	0.085	-0.025	-0.041	-0.050	-0.053	-0.165
P_i^0	情况②	-0.523	-0.565	-0.606	-0.623	-0.632	-0.637	-0.638	-0.696

Table 2

Key: (1)-(2) Condition.

In order to study the influence of Poisson ratio ν , we also made calculations of $\nu=0.5$ and $\nu=0.45$. The results are shown in Fig. 4.

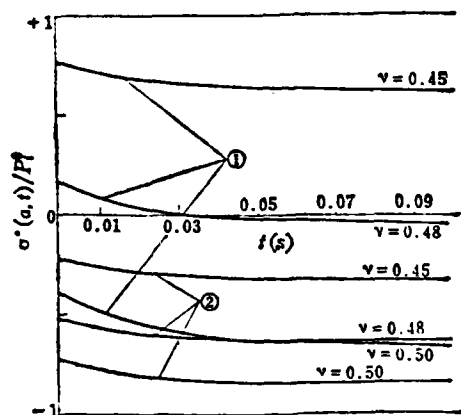


Fig. 4 $\sigma_0^*(a, t)$ under suddenly-applied pressure.

We used formulas (59) and (61) for the calculation of maximum strain $\epsilon_0^*(a, t)$ under two types of conditions. The results are given in Table 3 and Fig. 5. When calculating, we used $F(t) \approx 1/E(t)$.

$t(s)$	0	0.01	0.03	0.05	0.07	0.09	0.10	1	
$\frac{\varepsilon_0^*(a, t)}{P_i^0}$	情况①	0.81×10^{-3}	0.90×10^{-3}	1.03×10^{-3}	1.11×10^{-3}	1.16×10^{-3}	1.19×10^{-3}	1.20×10^{-3}	1.83×10^{-3}
	情况②	0.42×10^{-3}	0.46×10^{-3}	0.51×10^{-3}	0.54×10^{-3}	0.56×10^{-3}	0.57×10^{-3}	0.58×10^{-3}	0.83×10^{-3}

Table 3

Key: (1)-(2) Condition.

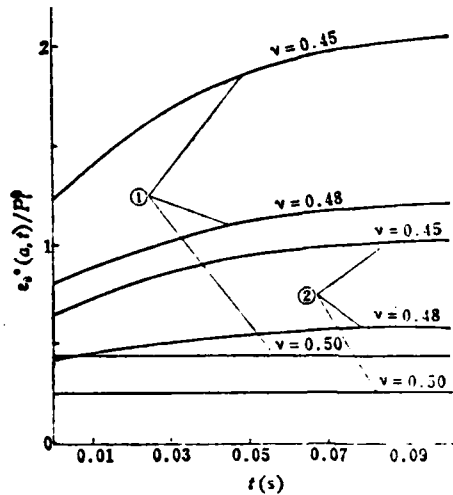


Fig. 5 $\varepsilon^*(a, t)$ under suddenly-applied pressure.

We can see from Figs. 4 and 5 that: under the first type of condition both the stresses and strains are higher than in the second type of situation, the stress decreases with the time, the strain enlarges with the time and they both tend to be limiting values; the influence of Poisson ratio ν of the propellant is very great on the stress and strain values.

2. Calculation results of gradually-applied pressure $P_i = 70[1 - \exp(-60t)]$:

We used formula (58) to calculate the maximum stress under two types of conditions first using formula (32) to calculate auxiliary function $f_E(t)$. The calculation results are listed in Table 4 and Fig. 6.

$t(s)$	0	0.01	0.03	0.05	0.07	0.09	0.11	1
$f_E(t)$	0	30.04	46.40	46.19	43.32	41.83	40.49	22.94
$\frac{\sigma_a^*(a, t)}{P_i^0}$ 情况①	0	0.054	0.040	0.025	-0.024	-0.010	-0.019	-0.164
情况②	0	-0.248	-0.489	-0.579	-0.614	-0.629	-0.635	-0.696

Table 4

Key: (1)-(2) Condition.

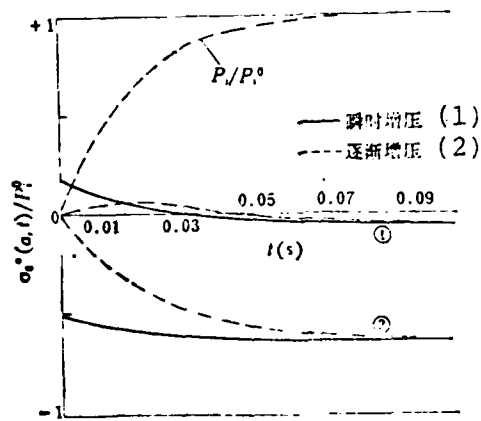


Fig. 6 $\sigma_{\theta}^*(a, t)$ and P_i (?) under gradually applied pressure.
Key: (1) Suddenly-applied pressure; (2) Gradually-applied pressure.

We used formula (50) to calculate auxiliary function $f_F(t)$ and then used formulas (60) and (62) to calculate the maximum strain under the two types of conditions. The calculation results are listed in Table 5 and Fig. 7.

$t(s)$	0	0.01	0.03	0.05	0.07	0.09	0.11	1	
$f_F(t)$	0	0.507	1.111	1.427	1.617	1.752	1.859	3.235	
$\frac{\varepsilon_{\theta}^*(a, t)}{P_i^0}$	情况①	0	0.39×10^{-3}	0.80×10^{-3}	0.99×10^{-3}	1.08×10^{-3}	1.15×10^{-3}	1.20×10^{-3}	1.82×10^{-3}
	情况②	0	0.20×10^{-3}	0.40×10^{-3}	0.49×10^{-3}	0.53×10^{-3}	0.56×10^{-3}	0.58×10^{-3}	0.82×10^{-3}

Table 5
Key: (1)-(2) Condition.

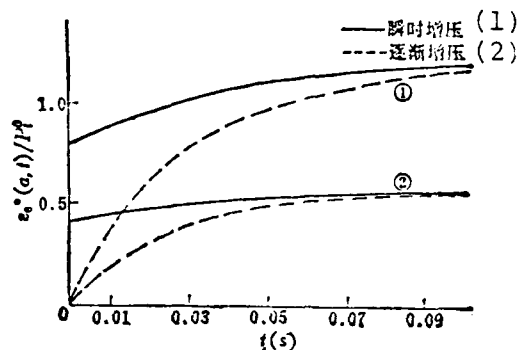


Fig. 7 $\epsilon_0^*(a,t)$ under gradually-applied pressure.

Key: (1) Suddenly-applied pressure; (2) Gradually-applied pressure.

We can see from Figs. 6 and 7 that: under the first type of condition, the stress gradually decreases from tensile stress to compressive stress and under the second type of condition it is compressive stress from beginning to end; under the second type of condition the strain is markedly lower than in the first type of condition; the stresses and strains gradually approach the value under suddenly-applied pressure following the time. When the internal pressure approaches the equilibrium pressure, the absolute value of the stress and the value of the strain are both slightly lower than the value of this time under suddenly-applied pressure. In engineering approximate calculations, estimations of the stresses and strains are allowable based on calculations under suddenly-applied pressure.

IV. Conclusion

1. We can see from the above examples that some of the existing engineering calculation methods assume that the propellant is an incompressible material ($\nu=0.5$) and the obtained stress and strain values tend to be low. In other calculation methods, they easily disregard the terms with F/E_c . We can see from formulas (57)-(62) that the calculation values also tend to be low, especially when the casing material's elastic modulus E_c is relatively low (e.g. aluminum alloy and glass fiber reinforced plastic casings). However, use of the method introduced in this paper can be used to simply, easily and quite accurately

calculate the stress and strain values under internal pressure loads.

2. The difference between the stresses and strains are very large under the two types of conditions. Under the second type of condition (the casing is in a planar strain state and the grains are in a common planar stress state), the stress and strain values are lowest. Therefore, during calculations, it is necessary to accurately calculate which type of stress state the grains and casing of the engine belong to. This conclusion also shows us that when designing an engine, we should as much as possible cause them to be in the second type of condition.

3. In order to accurately calculate the stress and strain values under internal pressure loading, it is necessary to have short time relaxation modulus data and accurate Poisson ratio data. Both the stresses and strains are very sensitive to the Poisson ratio: the smaller the ν value, the higher the stress and strain values; when the ν value increases to 0.5, the stress and strain values are lowest. Moreover, the strain does not change with the time under suddenly-applied pressure.

After obtaining the stress and strain values under internal pressure loading, the stress and strain values are coordinated during the solid cooling, storage, environmental change and transport etc. processes and we can then further carry out complete structural analysis of the propellant grains.

References

- [1] "Engineering Methods for Grain Structural Integrity Analysis" AD-408799.
- [2] Handbook for the Engineering Structural Analysis of Solid Propellants" AD-887428.
- [3] A.B. Boyd, W.M. Burkes and J.E. Medford, "Grain Design and Development Problems for Very Large Rocket Motors" Solid Propellant Rocket Research 1960.
- [4] M.L. Williams, "Structural Analysis of Viscoelastic Materials" AIAA J. Vol 2 No 5 1964.
- [5] M.L. Williams, "The Strain Analysis of Solid Propellant Rocket Grains" J. the Aero/Space Sciences Vol 27 1960.

(continued next page)

References (continued)

- [6] E.H. Lee, J.R.M. Radok and W.B. Woodward, "Stress Analysis for Linear Viscoelastic Materials" Transaction of the Society of Rheology III, 1959.
- [7] D.O. Ordehl, M.L. Williams, "Some Preliminary Photoelastic Design Data for Stresses in Rocket Grains" Jet Propulsion Vol 27 1957.
- [8] M.L. Williams, P.J. Blatz, "Fundamental Studies Relation to Systems Analysis of Solid Propellants" AD-256905.
- [9] anjing Engineering College, "Integral Transformation," People's Education Press, 1978.

A STUDY OF THE LOW FREQUENCY INSTABILITY OF THE SOLID PROPELLANT ROCKET ENGINE

Zhao Bohua

Abstract

This paper presents a new concept of the low frequency λ^* instability on the basis of experiments and analysis of the flow field of combustion gases in the engine. It shows the mutual relationship between the tubular grain design parameters (ratio of inside port to outside port parameter λ and the combustion chamber pressure p) and its effect on low frequency instability. A relational formula is derived through study for analyzing the low frequency instability of the tubular grain engine. The theoretical analysis agrees with the test results. This paper has reference value for selection of tubular grain design parameters (p and λ) and their inhibition of low frequency instability.

I. Introduction

Low frequency instability such as low frequency oscillation and surge is generally a nonacoustic oscillation problem. The p - t test curve of the pressure of commonly seen low frequency oscillation combustion and surge which changes with time is shown in Fig. 1.

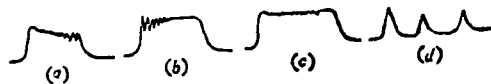


Fig. 1 p - t curve of low frequency oscillation and surge.

In the figure, (a) is the increased amplitude low frequency oscillation in the engine due to certain factors having very small vibration. At this time, amplitude lengthened index $s > 0$. (b) is the decreased amplitude low frequency oscillation combustion in the engine due to certain factors producing

certain amplitude fluctuations. At this time, amplitude attenuation index $s < 0$ which shows that the damping in the engine causes the oscillation to gradually weaken and finally tend towards stable combustion. (c) is the p-t curve of equal amplitude low frequency oscillation combustion when $s=0$.

(d) is the surge's p-t curve. There are two types of low frequency instability, linear and nonlinear. This paper studies the problem of linear low frequency instability with oscillation frequency of about 100Hz.

As regards the tubular grain engine, when the operating time of the engine is short and there are strict requirements,

$\lambda = \frac{x_{\text{inside}}}{x_{\text{outside}}} < 1$ is often used and at this time relatively large loading density can be obtained. Tests show that if the operating pressure of the combustion chamber is greater than the critical pressure value of this propellant and the λ value of the tubular grain is smaller than a certain λ^* , at the low of -40°C , low frequency instability combustion will occur.

This type of low frequency instability will cause the thrust to have relatively large fluctuations and changes. It also often causes rockets and missiles to have poor firing concentration at low temperatures and even the dropping of bombs. When the low frequency oscillation frequency is equal to the natural oscillation frequency of the rocket or missile system, this can result in the mechanical oscillation of the entire missile system or components causing the missile to be unable to operate normally. In certain strategic missile engines as well as in aerospace applications, because it is necessary to use the advantages of low combustion chamber pressure and to raise the specific impulse of the weight of the engine, study and resolution of this problem has important and real significance.

II. The Problem of Low Frequency λ^* Instability

If there is no heat loss in the solid phase of the propellant, its heat conduction control equation is

$$\frac{\partial T}{\partial t} = \alpha \frac{\partial^2 T}{\partial x^2} - r \frac{\partial T}{\partial x} \quad (1)$$

In the formula, $\alpha = \frac{K}{\rho_p C_p}$, ρ_p , C_p separately indicate the density specific heat and heat conduction coefficients of the solid propellant and r is the combustion rate of the propellant. The source point of the x axis is taken on the surface of the propellant as shown in Fig. 2.

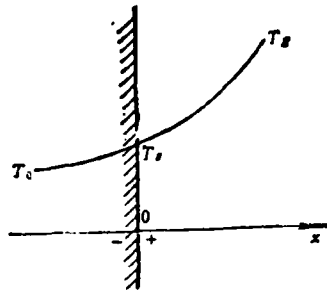


Fig. 2 Chart of the temperature distribution.

The boundary conditions are

$$x = -\infty, T = T_0$$

$$x = -0, T = T_s$$

$$\frac{\partial T}{\partial x} = H_s \text{ (temperature gradient when } x = -0)$$

Based on the above boundary conditions, by solving partial differential equation (1), we obtain the temperature distribution formula of the solid propellant grains when in a steady state

$$\bar{T} = \left(\frac{\alpha}{\bar{r}} \right) \bar{H} \exp \left[\left(\frac{\bar{r}}{\alpha} \right) x \right] + T_s \quad (2)$$

When $x = -0$ and $T = \bar{T}_s$ are substituted into formula (2), we obtain the grain surface temperature formula

$$\bar{T}_s = \left(\frac{\alpha}{\bar{r}} \right) \bar{H}_s + T_s \quad (3)$$

When in a steady state, the energy equilibrium relation in the solid propellant's grain surface area can be written as

$$K\bar{H}_s = K_s\bar{H}_{s,0} + \rho_s \bar{r} Q \quad (4)$$

In the formula, Q is the surface phase change heat.

When formula (4) is multiplied by $\bar{r}/K\bar{H}_s$ and substituted into formula (3), we obtain the expression of the grain's steady state combustion rate.

$$\bar{r} = \frac{\alpha}{K(\bar{T}_s - T_0)} (K_s\bar{H}_{s,0} + \rho_s \bar{r} Q) \quad (5)$$

Above, we obtained temperature \bar{T}_s of the solid propellant surface under a steady state condition as well as the theoretical expression of the grain's combustion rate r . If there are certain factors which cause the grain's surface temperature to change, it then necessarily directly influences the change of the grain's combustion rate and the change of the combustion rate will cause changes in the combustion chamber pressure.

As regards the tubular grain engine with $\lambda < 1$, because flow rates of the combustion gases of the inside port and outside port are not equal, the parallel gas flow of the outside port must be divided into two gas flows by the stagnation point and the position of the stagnation point is related to the size etc. of the λ value. Figure 3 shows the model of the combustion gas flow field in this type of engine. Because the combustion gas flows of the outer surface of the solid propellant's tubular grain flows backwards, under certain conditions, it possibly causes disturbance of the combustion gas flow in the vicinity of the stagnation point and the formation of helicon waves. It is thus necessary to irritate the grain surface in varying degrees. When the ratio of inside port to outside port parameter λ of a single tubular grain engine with double-base propellant is 0.6, at -40°C , the

combustion chamber's equilibrium pressure is 7.85MPa and the test curve of the low frequency oscillation pressure which changes with time is as shown in Fig. 4. When observed from the finally combusted grain, there are grain spots and ripples as well as the formation of inverted cones on the grain's outer surface of the grain's front end (far from the nozzle end). The final test proved the accuracy of the hypothesis of the combustion gas flow field model in the engine.

We can therefore simply describe this type of low frequency oscillation combustion as follows: under certain pressure conditions, when the λ value is smaller than a certain λ^* value, because of the backward flow of the combustion gas flow, a very small disturbance of the combustion gas flow will be caused near the stagnation point of the outer surface of the grain. The disturbance or oscillation of the gas phase in the engine can cause periodic changes in the heat conduction and temperature and the decomposition speed of the solid phase can be taken as the function of the periodic changes of the grain's surface temperature. Based on the feedback mechanism, the fluctuation of the combustion rate uses the fluctuation of the pressure caused by the combustion chamber's transfer function and the pressure fluctuation uses the feedback of the combustion's transfer function and the resulting fluctuation of the combustion rate. As a result, low frequency oscillation combustion can be produced in the solid propellant rocket engine.

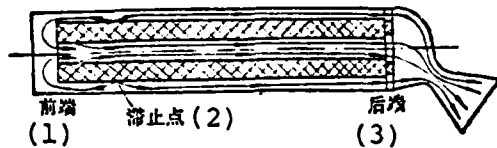


Fig. 3 Schematic of combustion gas flow field in engine when $\lambda < 1$.

Key: (1) Front end; (2) Stagnation point; (3) Rear end.

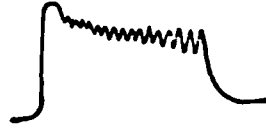


Fig. 4 Curve of low frequency oscillation pressure.

We know based on the energy conservation equation that in the combustion chamber the combustion gas produced from the surface of the propellant grain is equal to the mass flow flowing passed the nozzle as well as the sum of the changes of the combustion gas mass in the combustion chamber. That is

$$A_p \rho_g r = -\frac{C_D}{g} A_t p + \frac{d(\rho_g V_c)}{dt} = \frac{C_D}{g} A_t p + \rho_g \frac{dV_c}{dt} + V_c \frac{d\rho_g}{dt}$$

Because

$$\frac{dV_c}{dt} = A_v r, \quad \frac{d\rho_g}{dt} = \frac{1}{gRT_g} \frac{dp}{dt}$$

then

$$(\rho_g - \rho_s) A_v r = \frac{C_D}{g} A_t p + \frac{V_c}{gRT_g} \frac{dp}{dt} \quad (6)$$

In the formulas, A_p indicates the combustion surface of the grain; ρ_g and T_g separately indicate the density and temperature of the combustion gas; R is the gas constant; t is the time; C_D is the weight flow coefficient, V_c is the free volume of the combustion chamber; A_t is the nozzle throat area; g is the gravitational acceleration.

If low frequency oscillation combustion is produced in the engine as shown in Fig. 4, we assume the pressure amplitude of the combustion chamber assumes a sinusoidal shape. That is

$$p = \bar{p} - p_0 e^{i\omega t} \quad (7)$$

If the phase angle of the combustion phase of the propellant grain to the pressure low frequency oscillation lead is β , then

$$r = ap^n = a [\bar{p} - p_0 e'' \sin(\omega t + \beta)]^n$$

If we expand the right end series of the above formula and disregard the higher term, then

$$r \approx a [\bar{p}^n - n p_0 \bar{p}^{n-1} e'' \sin(\omega t + \beta)] \quad (8)$$

In the formula, \bar{p} is the pressure when there is steady state combustion; p_0 is the assigned initial moment pressure amplitude; a is the combustion rate coefficient; n is the pressure index; ω is the oscillation angle frequency; s is the amplitude lengthening index or attenuation index.

When $s > 0$, this shows that the pressure amplitude lengthens with time based on the index law; when $s < 0$, this shows that the pressure amplitude attenuates based on the index law.. At this time, s indicates the size of the low frequency oscillation damping; when $s=0$, this indicates equal amplitude low frequency oscillation.

By differentiating formula (7), we obtain

$$\frac{dp}{dt} = -(p_0 e'' \omega \cos \omega t + p_0 e'' s \sin \omega t) \quad (9)$$

Because combustion gas density ρ_g and propellant density ρ_p can be disregarded and not calculated by substituting formulas (7), (8) and (9) into formula (6), we obtain

$$\begin{aligned}
& -\frac{\bar{p}}{\bar{r}} \{ \bar{r} - a n p_0 \bar{p}^{n-1} e'' \sin(\omega t + \beta) \} \\
& = \bar{p} - p_0 e'' \sin \omega t - \frac{V_g}{C_D k T_s A_s} [p_0 e'' (\omega \cos \omega t + s \sin \omega t)] \\
& -\frac{\bar{p}}{\bar{r}} [a n p_0 e'' \bar{p}^{n-1} \sin(\omega t + \beta)] \\
& = p_0 e'' \left\{ \sin \omega t + \frac{V_g}{C_D k T_s A_s} [\omega \cos \omega t + s \sin \omega t] \right\}
\end{aligned}$$

Letting

$$\begin{aligned}
\tau &= \frac{V_g}{C_D k T_s A_s} & \text{时间常数 (1)} & (10) \\
\zeta &= a n p_0 e'' \bar{p}^{n-1} & \text{燃速扰动函数 (2)} & \\
\Phi &= p_0 e'' & \text{压力扰动函数 (3)} &
\end{aligned}$$

Key: (1) Time constant; (2) Combustion rate disturbance function; (3) Pressure disturbance function.

Then

$$\begin{aligned}
\frac{\bar{p} \zeta}{\bar{r} \Phi} \sin(\omega t + \beta) &= (1 + s\tau) \sin \omega t + \omega \tau \cos \omega t \\
&= [(\omega \tau)^2 + (1 + s\tau)^2]^{1/2} \sin(\omega t + \beta)
\end{aligned}$$

In the formula

$$\cos \beta = \frac{1 + s\tau}{[(\omega \tau)^2 + (1 + s\tau)^2]^{1/2}}, \quad \sin \beta = \frac{\omega \tau}{[(\omega \tau)^2 + (1 + s\tau)^2]^{1/2}}$$

After simplification, we obtain

$$\frac{\Phi / \bar{p}}{\zeta / \bar{r}} = \frac{1}{[(\omega \tau)^2 + (1 + s\tau)^2]^{1/2}} \quad (11)$$

Formula (11) indicates the relational formula of the combustion chamber's transfer function of the pressure fluctuation caused by the combustion rate fluctuation. By multiplying $\bar{r}^2/4a$ by τ in the formula, we obtain dimensionless time constant $\tau_n = \bar{r}^2 \tau / 4a$ and the critical time constant if there is no low

frequency oscillation combustion is $(\tau_n)_{cr}$, that is

$$(\tau_n)_{cr} = \frac{\alpha^2 \bar{p}^{2n} V_c}{4\alpha C_D R T_g A_i} \quad (12)$$

This dimensionless critical time constant reflects the properties of the solid propellant, the special features of the engine's structure, the design parameters of the grain and other major factors influencing low frequency instability. It is a comprehensive parameter.

We let

$$\frac{V_c}{A_i} = \frac{\pi \psi (D_i - D^2 + d^2) L}{4 A_i} \quad (13)$$

$$\lambda^* = \frac{x_n^{(1)}}{x_n^{(2)}} = \frac{D_i^2 - D^2}{Dd} \quad (14)$$

(2)

Key: (1) Inside; (2) Outside.

In the formulas, D_i is the inside diameter of the combustion chamber; D , d and L are separately the outside diameter, inside diameter and length of the grain; ψ is the correction coefficient taking into consideration the ignition space and grain supporting space in relation to free volume V_c ; $x_{outside}$ is the inside port parameter; λ^* is the characteristic ratio of inside port to outside-port.

We substitute formula (13) into formula (14) and letting $S_i = \pi D d L$ and $\eta = \frac{d}{D}$, we then obtain

$$\frac{V_c}{A_i} = \frac{\psi S_i (\lambda^* + \eta)}{4 A_i} \quad (15)$$

By substituting formula (15) into formula (12), we obtain

$$\lambda^* = \frac{16\alpha C_D T_g A_i (\tau_n)_{cr}}{\psi S_i \alpha^2} (p^*)^{-2n} - \eta \quad (16)$$

We can rewrite formula (16) as another equivalent form, that is, the lowest critical pressure p_{cr}^* which does not produce low frequency oscillation combustion

$$p_{cr}^* = \sqrt[2n]{\frac{16\alpha C_p RT_g A_s(\tau_g)}{\psi S_g a^2(\lambda^* + \eta)}} \quad (16)'$$

Formula (16) shows that the index relationship of λ^* and p^* have a $(-2n)$ linear relationship to the given solid propellant and tubular grain engine. In order to guarantee that low frequency oscillation combustion does not occur, the smaller the λ^* , the higher the required critical pressure value p_{cr}^* .

III. Analysis of Test Results

When a certain single double-base tubular grain engine $\lambda \approx 1$, at -40°C , the equilibrium pressure of the combustion chamber is 7.85MPa and the engine has stable combustion. Under other constant conditions, we carried out several types of experiments with λ values less than 1 and when the λ value was less than a certain λ^* value, then low frequency oscillation combustion occurred. The measured test curve is shown in Fig. 5.

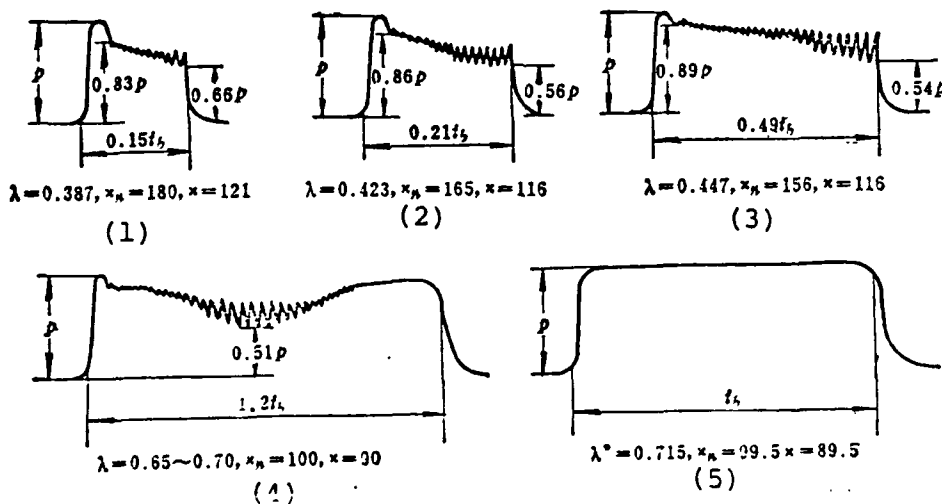


Fig. 5 p-t test curve when the double-base propellant is at -40°C , the pressure is 7.85MPa and there are different λ values.

Key: (1)-(5) Outside.

By analyzing the test results, we know that:

1. As regards a tubular grain engine with $\lambda < 1$, when the λ value is less than a certain λ^* value, at a low temperature of -40°C , low frequency oscillation combustion first occurs. Different trademark propellants have different λ^* values of low frequency oscillation combustion under the same combustion chamber pressure conditions. The larger the low frequency oscillation amplitude becomes, the lower the average pressure and when the pressure is lower than a certain value, combustion is extinguished or surges.

2. The smaller the λ value, the greater the pressure decrease loss Δp and the faster the time the grain cuts off combustion. The test curve of double-base propellant $\Delta p/p$ which changes with λ is shown in Fig. 6.

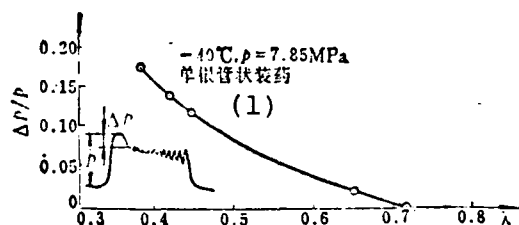


Fig. 6 Test curve of double-base propellant $\Delta p/p$ which changes with λ at -40°C .

Key: (1) Single tubular grain.

3. The measured low frequency oscillation frequency is about 100Hz, the low frequency oscillation frequency is almost unrelated to the size of λ^* and linearly increases with the base pressure (i.e. the lowest pressure between the adjacent pressure peaks). The amplitude of low frequency oscillation combustion generally decreases with the increases of the base pressure and thus the amplitude generally decreases with the increases of the frequency.

4. The smaller the λ^* value, the higher the lowest critical pressure value which does not produce low frequency oscillation combustion. It was observed in the tests that after low frequency oscillation combustion occurred, if we suitably raised the combustion chamber pressure or increased the λ value, this could eliminate the low frequency oscillation combustion. The partial test results of a double-base propellant tubular grain engine wherein λ^* changes with p^* at -40°C are shown in Fig. 7. The test results agree with theoretical formula (16).

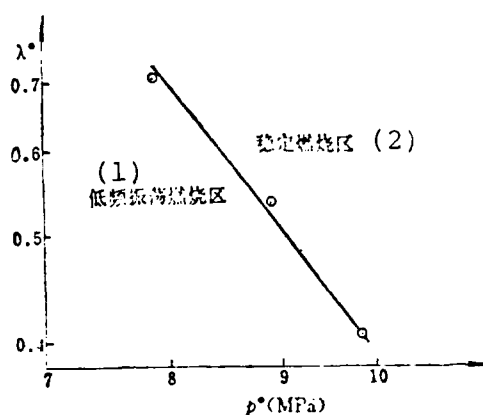


Fig. 7 Test curve of $\lambda^* - p^*$ of double base propellant tubular grain engine at -40°C .

Key: (1) Low frequency oscillation combustion area;
(2) Stable combustion area.

IV. Major Factors Influencing Low Frequency Instability

Low frequency instability has been observed when using common double base propellants, double-base propellants containing lead salt and metal additives as well as in other types of propellants; low frequency unstable combustion also occurred in engines with different types of grains such as end-burning grain, tubular grain, internal-burning star-shaped grain etc. The factors influencing low frequency instability are complex and we can know from formula (16) and analysis of the test results that the major factors influencing solid propellant rocket engine

instability are the composition and properties of the solid propellant, the grain's initial temperature, the structural characteristics of the engine and the grain's design parameters etc. We will present a simple analysis below.

1. Composition and Properties of the Solid Propellants

The low frequency instability and critical pressure values of solid propellants with different compositions are different. Generally, double-base propellants which do not contain metallic powder but have organic lead salt content and uniform distribution have marked effects on low frequency instability and the lower the content the worse its low frequency instability. Because organic lead salt is a type of combustion catalyst, under low pressure it has important regulating effects on the combustion rate of solid propellants. The catalytic effects are also related to the size of the organic salt so that the smaller the size, the more uniform the distribution in the absorbed grain and the better the catalytic effects.

The addition of aluminum powder or another metal as well as metal oxide is a good method for inhibiting low frequency oscillation combustion yet it also has its disadvantages in its effects on low frequency instability. Because the reaction heat of metallic oxide is quite high, under low temperatures, it can help solid propellant thermal decomposition and accelerate the combustion process. Aside from this, light metals are effective for inhibiting the pressure disturbance of the combustion process. If the grain size and contents of the metallic powder in the solid propellant are unsuitable, low frequency oscillation combustion can occur during combustion because of the periodic falling off of the accumulated metal from the propellant surface.

2. Initial Temperature of Grain

Given that other conditions are the same, it is much easier for low frequency unstable combustion to occur when the grain is

at a low temperature than when at normal and high temperatures. This is because when at high and normal temperatures, the combustion chamber pressure is generally larger than the pressure at low temperatures. The higher the pressure the larger the combustion gas density and the larger the damping effect on the initial disturbance in the combustion gases. Raising the pressure has important effects on inhibiting the low frequency oscillation combustion caused by pressure disturbance. Therefore, for a specific engine, it is only necessary that it not have low frequency oscillation combustion at low temperatures and then it will have stable combustion at normal and high temperatures.

3. Structural Properties of the Engine and the Grain's Design Parameters

The influence of the structure of the engine on low frequency instability is very complex. For example, when other conditions are constant, the low frequency stability performance of reverse flow multiple nozzle single grain engines is better than that of direct flow single grain engines. This is also to say that under the same pressure conditions, the λ^* of the former is smaller than that of the latter or that under the same λ^* value conditions the allowable critical pressure p^* value of the former is lower than that of the latter. Because of the complexity of the problem, at present, there is still no way of theoretically calculating the influence of the structural properties.

Different grain types have different influences on low frequency combustion instability. Tests show that the critical pressure of end-burning grain engines is much lower than that of other grain type engines because the combustion of end-burning grain is not influenced by the flow rate of combustion gas and the geometric parameters of the grain shape. Therefore, under the same pressure conditions, similar propellants are stable in end-burning grain engines. However, they can become unstable in tubular or star-shaped grain engines. This is then the influence

of the grain type's geometric parameters on low frequency instability. Internal-burning star-shaped grain also possibly has rotation similar to a vortex flow in a star-shaped cavity as shown in Fig. 8.

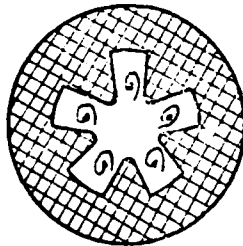


Fig. 8 Vortex flow of star-shaped cavity.

Under certain conditions, this type of rotation must in varying degrees puncture the inside surface of the grain and cause periodic fluctuations of the solid propellant grain's surface temperature and combustion rate. This can bring about low frequency unstable combustion and the star-shaped grain's geometric parameters are naturally also an important factor causing low frequency instability.

The larger the grain's port parameter x , the higher the critical pressure value; under certain pressure conditions, the larger the x value the higher the allowable λ^* value, yet its level of influence is not great.

To sum up, the critical pressure needed to guarantee that a tubular grain engine does not have low frequency instability is generally related to the solid propellant's type (SP), the lowest operating temperature ($-T$), the grain's design parameters and the structural properties of the engine (CC) etc. Therefore,

$$p^* = f_1(\text{SP}, -T, x, \lambda^*, \text{CC}) \quad (17)$$

As regards given solid propellants, the lowest critical

pressure for tubular grain engines with $x \leq x^*$ and $\lambda < 1$ not to have low frequency unstable combustion can be simplified and expressed as

$$p_{-T}^* = f_2 \left[\left(\frac{1}{\lambda^*} \right)^{\frac{1}{2n}} \right] \quad (18)$$

Each type of solid propellant can obtain a p_{-T}^* curve which changes with λ^* from tests. If low frequency unstable combustion occurs during the development process of the product, we can know from formula (16)' or formula (18) that it is only necessary to suitably raise the value or pressure p value to be able to completely inhibit low frequency unstable combustion.

References

- [1] R. Akiba and M. Tanno, Low Frequency Instability in Solid Rocket Motors, pp. 74-82, Proceedings of the First Symposium (International) on Rockets and Astronautics, Tokyo, 1959.
- [2] Robert Sehgal and Leon Strand, A Theory of Low-Frequency Combustion Instability in Solid Rocket Motors, AIAA Journal, Vo. 2, No. 4, 1964, 4.
- [3] R.A. Yount and T.A. Angelus, Chuffing and Nonacoustic Instability Phenomena in Solid Propellant Rockets, AIAA, 7, 1964.
- [4] N. Kubota, J. Kimura, Low Frequency Instability of High Pressure Exponent Double-Base Propellant, AIAA Paper No. 76-668.
- [5] R.S. Boer and H.F.R. Schoyer, Results of L^* -instability Experiments with Double-Base Rocket Propellants, N 78-13240.
- [6] T'ien, J.S., Sirignano, W.A. and Summerfield, M., Theory of L^* -star Combustion Instability with Temperature Oscillations, AIAA. J. Vol. 8, No.1, pp. 120-126, Jan. 1970.

IGNITION AND INITIAL PRESSURE PEAK OF SMALL SOLID PROPELLANT ROCKET ENGINES

Chen Hongzhang and Jia Qingying

Abstract

This paper mainly studies the causes of the initial pressure peak of small solid propellant rocket engines which form at high temperatures, proposes a specific method for predicting the ignition pressure peak and discusses the specific measures for eliminating or reducing the initial pressure peak at high temperatures. These studies are of practical significance to further improvements of the design of solid rocket engines and raising their overall performances.

Table of Symbols

C_q	: correction coefficient of flow of engine
$F(k)$: specific heat ratio function of mixed combustion gases of propellant and black powder
$F'(k)$: specific heat ratio of combustion gases of black powder
A_t	: nozzle throat area
P_c	: combustion gas pressure in combustion chamber
P_{ig}	: ignition pressure in combustion chamber when there is grain ignition
P_m	: maximum ignition pressure
$P_{c,m}$: pressure when combined combustion period is completed
P_k	: pressure in combustion chamber when grain is burned up
$P_{c,eq}$: equilibrium pressure of combustion chamber
C_g	: heat loss coefficient
f	: constant volume powder power of propellant
f_p	: constant pressure powder power of propellant
f_{ig}	: constant volume powder power of black powder
f_{pig}	: constant pressure powder power of black powder
f_k	: constant pressure powder power of mixed combustion gases
ρ_p	: density of propellant
ρ_k	: density of mixed combustion gases
Δ	: loading density of propellant in combustion chamber

s : grain's combustion surface area
 s_o : grain's initial combustion surface area
 u : propellant's combustion rate
 t_{ig} : ignition time of propellant
 t_m : time the maximum ignition pressure occurs
 t_k : time the grain combustion finishes
 t_{ml} : time corresponding to P_{ml}
 t : any given time in operation of combustion chamber
 m_p : production quantity of combustion gases of propellant
 γ_p : pressure peak ratio
 m_{ig} : production quantity of black powder gases
 \dot{m}_p : production rate of propellant's combustion gases
 \dot{m}_{ig} : production rate of black powder gases
 V_o : initial free volume of combustion chamber
 u_1 : combustion rate coefficient of propellant
 n : combustion rate pressure index of propellant
 L : length of combustion chamber
 L_1 : propellant's grain length
 D : inside diameter of combustion chamber
 D_1 : outside diameter of grain
 d : inside diameter of grain
 A_p : end free port area of grain
 x : ratio of initial combustion surface area and grain's end free port
 δ : meat thickness at any given time grain burns out
 $\delta_{c,m}$: meat thickness of burn out when combined combustion period is completed
 β : mass fraction
 k_k : specific heat ratio of mixed gases
 k_1 : specific heat ratio of black powder gases
 k_p : specific heat ratio of propellant's gases

I. The Combustion Properties of Black Powder and the Ignition State of the Engine

1. Combustion Properties of Black Powder

Based on experimental research on the combustion properties

of black powder, we consider that:

(A) The combustion rate of black powder is very fast and when the black powder flows passed the nozzle and there is not a great loss (aside from when black powder is placed on one end of the nozzle), the maximum ignition pressure point in the engine's ignition pressure curve is the finishing point of the combustion of the black powder.

(B) There is very little influence of environmental pressure on black powder combustion.

2. Ignition State of the Engine

(A) Optimum Ignition State

The optimum ignition state is when the ignition pressure in the engine reaches maximum value, the initial combustion surface of the entire propellant is ignited. Naturally, under these circumstances, the pressure establishment process of the combustion chamber is ideal and it can produce an ignition pressure peak.

(B) Early Ignition State

Early ignition of an engine points to the complete igniting of the propellant's combustion surface occurring far before the ignition pressure reaches the maximum ignition pressure. In this type of situation, there exists in the pressure establishment process of the combustion chamber the combined combustion period of black powder and propellant. Its existence is mainly due to the formation of the ignition pressure peak. Because the propellant requires different ignition energy under different initial temperatures and the ignition powder quantity generally used for the engine is difficult to change, the ignition of the small solid engine under high temperatures is in a serious early ignition state which is difficult to avoid. Figure 1 shows the pressure time curve of the early ignition engine.

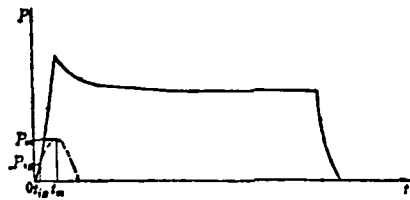


Fig. 1 Pressure time curve of an engine in early ignition state.

II. Prediction of Ignition Pressure Peak

1. Basic Formulas for Calculating Pressure in Combined Combustion Period

The process of pressure change in the combustion chamber of a solid rocket actually shows the contradictory process between the production and elimination of combustion gases. This paper begins from actual engineering applications, disregards some factors of secondary importance and proposes the following assumptions for the operating process of the combined combustion period of the solid rocket engine:

(A) The temperature and pressure of the combustion gases in the entire combustion chamber's free volume are uniform.

(B) The combustion gases in the combustion chamber can be used for ideal gas processing.

(C) The ignition of the entire initial combustion surface occurs simultaneously.

(D) The exhaust of the nozzle is only carried out at the speed of sound.

Based on the principle of the conservation of mass in the

combined combustion period, the production quantity of combustion gas should be equal to the combustion gas flow passed the nozzle in addition to the change rate of the stored quantity of combustion gases in the combustion chamber. We use the following equation to express it

$$p_p su + \dot{m}_{ig} = \frac{C_g F(k) A_i P_g}{\sqrt{C_g f_k}} + p_p su + \frac{V_0}{C_g f_k} \frac{dP_g}{dt} - \frac{P_g V_0}{(C_g f_k)^2} \frac{d(C_g f_k)}{dt} \quad (1)$$

After transposition and disregarding small quantity of high order, we obtain

$$\frac{dP_g}{dt} = \frac{C_g f_k}{V_0} \left[\dot{m}_{ig} + p_p su - \frac{C_g F(k) A_i P_g}{\sqrt{C_g f_k}} + \frac{P_g V_0}{(C_g f_k)^2} \frac{d(C_g f_k)}{dt} \right] \quad (2)$$

Here, the focus of analysis is on the expression of the propellant's combustion. It is well known that under non-corrosion effects (e.g. end combustion), its combustion rate formula can be expressed by $u = u_1 p_c^n$. However, in an engine with serious corrosive combustion, the combustion rate on different surfaces of the propellant is the function of the pressure and is also related to the gas flow rate etc. in this area. Tests show, however, that as regards small solid engines, especially engines with end combustion and side combustion engines under $L/D \leq 4 \leq A_p/A_t$ conditions, we need not consider the influence of corrosion effects on the combustion rate. When carrying out combustion chamber P-t curve pressure calculations, we can still use the previously given combustion rate formula. When carrying out integration operations in a relatively large pressure range, we should select a corresponding combustion rate formula with a different pressure range in a different pressure area of the integration.

2. Calculation of the Combustion Chamber's Internal Pressure in the Combined Combustion Period

(A) Determination of the Thermophysical Properties of the Mixed Gas

In order to approximately determine the main thermophysical properties of the mixed gas, we now introduce a simplified formula to determine mixed gas powder power f_k [1]

$$f_k = \frac{(1-\beta)f_{ig} + \beta f_p}{k_k}$$

In the formula

$$k_k = (1-\beta)k_i + \beta k_p$$

$$\beta = \frac{m_p}{m_p + m_{ig}}$$

From the above formula, we can easily determine the values of powder power f_k and specific heat ratio function $F(k)$ of the mixed gas at different moments during the combined combustion period.

(B) Determination of the Gas Production Rate of Black Powder
Figure 2 is the ignition pressure curve of a common engine.

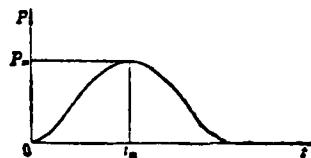


Fig. 2 Ignition pressure time curve.

In the figure, the rising section can be approximately expressed mathematically as

$$P(t) = -\frac{2P_m}{t_m^2}t^2 + \frac{3P_m}{t_m^2}t^3$$

When there is only black powder combustion, the ignition pressure in the combustion chamber and the production quantity of

the black powder gas have the following relationship

$$\dot{m}_{ig} = \frac{C_g F'(k) A_t}{\sqrt{C_g f_{pi_g}}} P(t) + \frac{V_0}{C_g f_{pi_g}} \frac{dP(t)}{dt}$$

After substituting in $P(t)$ and $\frac{dP(t)}{dt}$, we obtain

$$\dot{m}_{ig} = \frac{C_g F'(k) A_t}{\sqrt{C_g f_{pi_g}}} \left(-\frac{2P_m t^3}{t_m^3} + \frac{3P_m t^2}{t_m^2} \right) + \frac{V_0}{C_g f_{pi_g}} \left(-\frac{6P_m t^2}{t_m^3} + \frac{6P_m t}{t_m^2} \right)$$

Because the influence of environmental pressure during black powder combustion is very small, the expression of the production rate is still suitable in the combined combustion period.

(E) Establishment of a Set of Differential Equations

By substituting the expression of \dot{m}_{ig} into formula (2), we can obtain

$$\begin{aligned} \frac{dP_g}{dt} = & \frac{C_g f_k}{V_0} \left[\frac{C_g F'(k) A_t}{\sqrt{C_g f_{pi_g}}} \left(-\frac{2P_m t^3}{t_m^3} + \frac{3P_m t^2}{t_m^2} \right) + \frac{V_0}{C_g f_{pi_g}} \left(-\frac{6P_m t^2}{t_m^3} \right. \right. \\ & \left. \left. + \frac{6P_m t}{t_m^2} \right) + \rho_p s u_1 P_c^n - \frac{C_g F(k) A_t P_g}{\sqrt{C_g f_k}} + \frac{P_g V_0}{(C_g f_k)^2} \frac{d(C_g f_k)}{dt} \right] \end{aligned}$$

It is now still impossible to carry out numerical integration of this differential equation because under certain circumstances we only know the function relation of combustion surface s and meat thickness δ but are unclear of the function relation of s to t . For this reason, it is necessary to add two sets of equations to form a set of differential equations so as to attain an integral solution. Because

$$d\delta = u dt = u_1 P_c^n dt, \quad \frac{d\delta}{dt} = u_1 P_c^n,$$

therefore

$$\frac{ds}{dt} = \frac{ds}{d\delta} \frac{d\delta}{dt} = u_i P_i^* \frac{ds}{d\delta}$$

Integral initial values s and δ of the set of differential equations of the combined combustion period both use the grain's initial combustion area s_0 and initial combustion meat thickness $\delta = 0$. At present, the integrated pressure initial value P_{ig} and the time of ignition t_{ig} can only be determined by an approximation method.

On the basis of the above given set of differential equations of the combined combustion period's pressure change pattern, we wrote a computer program to predict the engine's initial pressure peak and separately carried out prediction calculations of the ignition pressure peak of engines with certain products. The results and test values are basically in agreement.

III. Factors Influencing the Ignition Pressure Peak

It is not difficult to see from the above set of differential equations that in a small solid rocket engine with very little corrosive combustion, the existence of the production rate of black powder is the major factor influencing the initial pressure peak. We call the initial pressure peak formed because of this the ignition pressure peak and call the initial pressure peak formed from corrosive combustion the corrosion pressure peak. Under normal conditions, the initial pressure peak of the engine is composed of these two parts. Tests prove that in small solid rocket engines with rational designs, corrosive combustion can often be very small and thus need not be considered. However, for a small engine which uses black powder ignition, the ignition pressure peak that appears at high temperatures is difficult to avoid. Therefore, generally speaking, the ignition pressure peak is the main part making up the initial pressure peak of the

small solid engine at high temperatures.

This type of pressure rise is usually expressed by peak value ratio γ_p and at present the high temperature peak value ratio of most small solid engines which use black powder ignition is in the 1.4-2.0 range. This can be even higher in special situations.

In order to investigate the various factors influencing the ignition pressure peak and find a method for decreasing or eliminating the ignition pressure peak, we wrote a computer program to carry out a relatively large number of simulated calculations of the engine's ignition pressure peak and to study the influence of the engine's design parameters on the high temperature ignition peak. The calculation results agreed with the phenomena observed in the experimental research on the engines.

1. Properties of the Propellant

When guaranteeing conditions wherein the engine has reliable low temperature ignition, the larger combustion rate pressure index n of the engine at high temperature, the larger the high temperature ignition pressure peak. At high and low temperatures, the larger the difference of the ignition energy required by the engine on the unit combustion surface area, the larger the ignition pressure peak of the engine at high temperatures. However, because the present propellant tests and employed separation are more serious, this problem has yet to receive enough attention and it is still not regarded as an important performance indication of the engine. This is worthy of attention.

2. The Loading Density of the Engine

When guaranteeing conditions of reliable low temperature ignition in engines which use the same solid propellant, the larger the loading density of the propellant in the combustion chamber (the smaller the initial free volume), the higher the ignition pressure peak of the engine at high temperatures.

Therefore, as regards a certain type of propellant, in order to prevent the formation of an excessively large ignition pressure peak at high temperatures, we should limit the loading density of the propellant in the combustion chamber.

In order to resolve the problem of a certain engine having a high initial pressure peak at high temperatures and sunken initial section pressure at low temperatures, we carried out a large number of ignition tests. The results proved that at high temperatures the engine's initial pressure peak noticeably changed with the loading density of the combustion chamber. At the same time, the test phenomena also showed that after the initial free volume of the engine was smaller than a certain determined value, at high temperatures the engine's initial pressure peak drastically changed with the reduction of the initial free volume. When the initial free volume changed in another relatively large range, at high temperatures the engine's initial pressure peak changes were relatively mild. Therefore, in engine's with relatively large loading densities, we should control the tolerance of the combustion chamber's initial free volume and then we will be able to ensure that the engine's initial pressure peak is stable at high temperatures.

Although the loading densities of propellants in greatly reduced engine combustion chambers can eliminate the ignition pressure peak at high temperatures, yet this will cause the loading quantity of the propellant to greatly decrease. Therefore, when using this method to decrease the engine's ignition pressure peak, we must consider it comprehensively.

3. Design Parameter of the Engine - Surface-to Throat Ratio R_{ot}

It is common that when the other parameters of the engine are constant, the larger the surface-to-throat ratio R_{ot} , the smaller the peak value ratio at high temperatures. However, an excessively

large R_{ot} causes the maximum pressure to increase and thus increases the negative weight; on the contrary, if the R_{ot} is excessively small, this can only cause γ_p to markedly increase but can also influence the release of propellant energy because the equilibrium pressure is excessively low. Therefore, as regards each type of solid propellant, when designing engines, it is necessary to select a moderate R_{ot} value under totally allowable conditions and this will then be able to benefit the raising of the overall performance of the engine.

4. Proper Ignition Design Has Certain Effects on Lowering the Engine's High Temperature Ignition Pressure Peak

(A) Use of High Energy Ignition Powder

High energy ignition powder generally has a low combustion rate pressure index, small gas content and high heat value, it has very strong energy output in an infrared area, it can have various production prescriptions and grain compositions, it is an effective igniter and there is a tendency under many conditions to replace the black powder with a high energy igniter. Its use can to a certain extent lower the engine's ignition pressure peak and improve the low temperature ignition performance.

(B) Revising the Structural Form of the Ignition Design

The ignition energy required on the ignition unit surface area for different types of propellants under the same initial temperature are different. At the same time, during the ignition process, the heat response time required to establish a normal heating layer on the propellant's surface is also different (for the majority of propellants, the suitable response time is usually in the 5-20ms range). When the ignition powder is a certain quantity and the heating time of the black powder gas is either too short or too long on the propellant's surface, these are disadvantageous to the normal ignition on the propellant's surface. When carrying out ignition design of engines with different types of grains, we should distinguish the different

conditions and suitably select the black powder's quantity, size, type of igniter and location of the igniter etc. so as to obtain optimal ignition effects.

If static tests of a certain engine show that, given the other conditions are the same, when using a celluloid ignition box, the bursting pressure of the box is low and the initial section of the engine's P-t curve has a relatively smooth rise. When using an aluminum ignition box, the bursting pressure of the box is high, the initial section of the engine's P-t curve assumes a saddle shape and the maximum pressure at high temperatures is about 10-15% higher than when using a celluloid box. We can see that good ignition design has certain effects on lowering the ignition pressure peak of engines at high temperatures.

IV. Experimental Research on Eliminating the Ignition Pressure Peak

On the basis of specialized experimental research, we propose a new ignition design method. In small solid engines with not very serious corrosive combustion, use of this method can effectively eliminate the initial pressure peak of the engine at high temperatures under conditions wherein the engine grain is not reduced and there is no increase of the negative weight and thus improve the overall performance of the engine.

The procedure of the new design method is as follows:

1. In developing the grain engine, we begin from the requirements of low temperature reliable ignition and not having a relatively large ignition pressure peak at high temperatures, and carry out predictions and calculations of the new ignition material and structural design.

2. When using false grain in the engine, we measure the actual ignition pressure's time curve in the engine to examine

whether or not it has reached the predicted design requirements of the original igniter. It is necessary to make revisions on the original ignition design until the ignition design reaches design requirements.

3. On the basis of the two operations mentioned above, we carry out ignition tests of the real engine and measure the P-t curve of the engine.

This new ignition design method has already been applied in certain engines. Figures 3 and 4 separately show the P-t curves of engines at high and low temperatures when using the new ignition design and when using the common ignition design. It is not difficult to see from the curves that in using two different types of ignition designs in the same engine, when we are able to guarantee low temperature reliable ignition and stable combustion, there is a marked difference in the pressure curves of the engine at high temperatures. When using the new ignition design method, the peak value of the engine's pressure curve at high temperatures is relatively small, $\gamma_p = 1.08$ (approximately), while when using the common ignition design, the peak value of the pressure curve at high temperatures is more than 1.56 higher than γ_p .

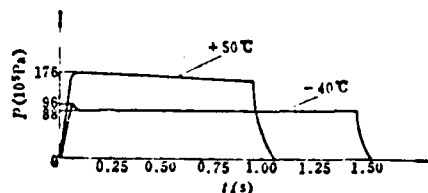


Fig. 3 Pressure time curves of a certain engine when using the new ignition design.

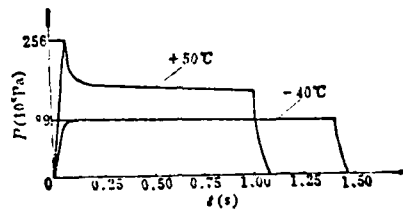


Fig. 4 Pressure time curves of a certain engine when using the common ignition design.

Comparisons of ignition tests on real engines show that the new ignition design method has marked effects on raising the overall performance of engines, it has a simple structure, reliable operations and use is convenient etc. It can be used on small solid engines and it is also easy to realize on rocket weapons with finalized designs.

References

- [1] Е. Б. ВОЛКОВ, Т. А. СЫ РИЧЫН, Г. Ю. МЗИНГ, СТАТИКА И ДИНАМИКА РАКЕТНЫХ ДВИГАТЕЛЬНЫХ УСТАНОВОК В ДВУХ КНИГАХ I, МОСКВА. «МАШИНОСТРОЕНИЕ». 1978.
- [2] "Basic Problems of Solid Propellant Rocket Engines," F.A. Williams et al, Translated by Jin Guqun, National Defense Publications, 1977.7.

END

FILMED

9-84

10-84